WILEY-VCH

Ligand Circuit Concept for Developing Gas Separation Materials from Pore-Space-Partitioned Metal-Organic Frameworks

Natalie Tran,[a] Wei Wang,[b] Yichong Chen,[b] Pingyun Feng,*[b] Xianhui Bu*[a]

Natalie Tran, Xianhui Bu
Department of Chemistry and Biochemistry, California State University Long Beach, Long Beach, CA 90840, United States
E-mail: xianhui.bu@csulb.edu

Wei Wang, Yichong Chen, Pingyun Feng
Department of Chemistry, University of California, Riverside, Riverside, CA 92521, United States
E-mail: pingyun.feng@ucr.edu

Abstract:

Isoreticular chemistry is among the most powerful strategies for designing novel materials with optimizable pore geometry and properties. Of great significance to the further advance of isoreticular chemistry is the development of broadly applicable new concepts capable of guiding and systematizing the ligand-family expansion as well as establishing correlations between dissimilar and seemingly uncorrelated ligands for better predictive synthetic design and more insightful structure and property analysis. Here we propose ligand circuit concept and its use for the synthesis of a family of highly stable, high-performance pore-space-partitioned materials based on an acyclic ligand, *trans*, *trans*-muconic acid. This work represents a key step towards developing highly porous and highly stable pore-space-partitioned materials from acyclic ligands. The new materials exhibit excellent sorption properties such as high uptake capacity for CO_2 (81.3 cm^3/g) and C_2H_2 (165.4 cm^3/g) by CPM-7.3a-NiV. CPM-7.3a-CoV shows C_2H_6-selective C_2H_6/C_2H_4 separation properties and its high uptakes for C_2H_4 (134.0 cm^3/g) and C_2H_6 (148.0 cm^3/g) at 1 bar and 298 K contribute to the separation potential of 1.35 mmol/g. The multi-cycle breakthrough experiment confirms the promising separation performance for C_2H_2/CO_2.

1. Introduction

Isoreticular chemistry is a synthesis strategy for creating new framework materials and modifying pore geometry and properties by changing framework building blocks without changing the framework topology.[1] As such, the starting point of isoreticular chemistry is the creation or selection of a good structural platform. Once a platform is chosen, the choice of a suitable ligand is the most commonly used isoreticular strategy. Thus developing new strategies for identifying isoreticular ligands is among the most important aspects of isoreticular chemistry. Whether two ligands are isoreticular ligands (ligands giving rise to isoreticular frameworks) depend on MOF platforms. For example, two ligands that are isoreticular on a two-module MOF platform (one inorganic node and one organic node) may not be isoreticular on a multi-module MOF platform due to additional requirements on a multi-module platform such as the range of length ratios between two types of ligands. Another example is that different MOF platforms have different propensity for the formation of interpenetrating frameworks so that a longer ligand can achieve isoreticular chemistry on one platform while forming interpenetrating frameworks on another MOF type.

Researchers have come up with a variety of approaches to accomplish this ligand-based isoreticular process, each with a different level of success depending on the MOF structure type. Some common ones involve (1) introducing one or more substituent groups with different chemical properties and steric hinderance (the substituent approach),[2] (2) changing the length (the extender approach), width (similar to the introduction of functional groups), or thickness (sometimes called the 3-D ligand approach) of the ligand core or backbone,[3-4],[5] and (3) changing the relative orientation between functional groups (e.g., through rotation of a functional group around the metal-ligand bonding vector) or the angle between metal-ligand bonding vectors.[6] Other approaches are based on the introduction of one or more heteroatoms located either in (4) the non-binding parts (the heterocore approach, e.g., triazine core vs. pyridine core)[7] or (5) in the binding parts (the functional-group approach, e.g., -COO and pyrazolate/triazolate/tetrazolate can coordinate to M_3OH trimer in the same way).[3] Recently, with the intention of maintaining

isoreticular chemistry while providing a greater degree of control over pore property, we proposed the use of (6) bioisosteric (BIS) replacement strategy for the MOF ligand expansion.[8] The BIS concept for MOFs is inspired by the drug design method which involves replacing benzene rings with other scaffolds while maintaining the overall directions of the bonding vectors.[9] The BIS concept usually involves the change of the hybridization states (from sp^2 to sp^3) of all or some carbon atoms of the ligand.

Establishing the correlation between ligands (especially those chemically or structurally dissimilar and seemingly unrelated ones) can help isoreticular chemistry from the pre-synthesis planning and design stage to the after-synthesis structure-property analysis stage. Some relationships between ligands are obvious and some are less so. For all ligands used in MOFs, there are one, two, or more paths (called circuits here) when going from one functional group to another one.[10] In addition to the number of circuits and their lengths (in terms of the number of non-hydrogen atoms), each circuit can vary by the presence/absence of carbon atoms with different hybridization states or heteroatoms (the related ratio between the numbers of saturated/unsaturated bonds or sp^3-C/sp^2-C ratio). For example, for 1,4-benzenedicarboxylate (bdc), there are two equivalent paths involving four sp^2-carbon atoms between two COO- groups (**Scheme 1**). Ligand expansion starting from a bdc-based MOF platform can be achieved by slicing the original bdc ligand to reduce the number of circuits (the ligand scissoring concept). In the opposite manner, it is also conceivable to add one or more circuits (e.g., from bdc to bco, bco = bicyclo[2.2.2]octane-1,4-dicarboxylate). This idea involving removal and addition of circuits are collectively called the ligand circuit concept. Ligands that are related by ligand circuit concept are called correlated ligands which may or may not function as isoreticular ligands depending on the MOF platform. To be broadly useful and out of necessity in some cases, the ligand circuit concept includes the scenarios involving a simultaneous change in the hybridization states of some or all carbon atoms, as well as heteroatom replacement.

In addition to serve as a practically applicable method to derive or identify suitable ligands for isoreticular chemistry, the ligand circuit concept has the benefit of establishing the correlation

between different ligands that may appear to be unrelated. For the design of new materials, the knowledge of the ligand-circuit relationship can have predictive values (especially in multi-module system) with respect to the resulting unit cell parameters, pore geometry, possible matching or mismatching between different ligand modules (e.g., the length ratio between two types of ligands). The ligand circuit concept can be particularly helpful in the design of multi-module MOF materials in which the geometric relationship between different ligand types needs to be taken into consideration to achieve isoreticular assembly.

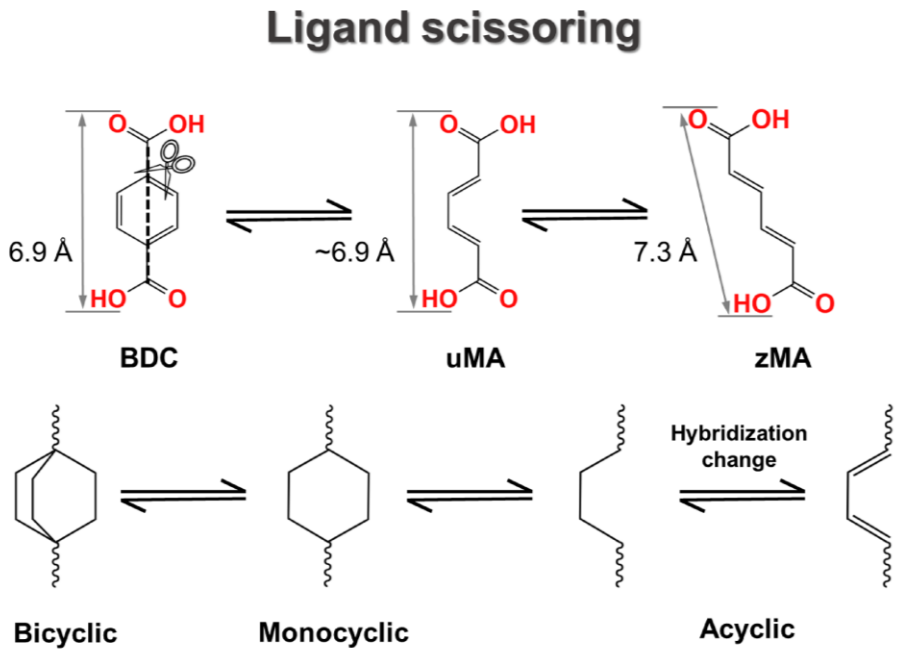

Scheme 1. Ligand circuit concept for establishing the family of correlated ligands and for isoreticular MOF design and analysis. The scissoring of the common BDC ligand results in u- and z-shaped MA (uMA or zMA) ligands capable of being used in the construction of isoreticular *pacs*-MOF materials.

Here, we report the development of a new family of *pacs* MOF materials based on *trans*, *trans*-muconic acid (H_2MA, $C_6H_6O_4$, denoted as L1 ligand) which is a benzene-related molecule (e.g., metabolite of benzene in human). The MA ligand (sp^3-C/sp^2-C ratio = 0, 2 C=C and 1 C-C in the

4-carbon backbone) is one of several possible ligands when the ligand circuit concept (ligand scissoring approach) is applied to 1,4-benzenedicarboxylate (bdc). A total of 9 isoreticular *pacs* materials have been synthesized by using 3 types of pore-partition ligands (denoted as L2 ligands, a = tpt = 2,4,6-tri(4-pyridyl)-1,3,5-triazine, b = tppy = 2,4,6-tri(4-pyridyl)pyridine, and c = tpbz = 1,3,5-tri(4-pyridyl)benzene) and 7 types of M3 metal trimers (Co, Fe, MgV, CoV, NiV, CoFe, CoIn) (**Figure 1**). The new *pacs* materials exhibit excellent sorption properties such as high uptake capacity for CO_2 (81.3 cm^3/g) and C_2H_2 (165.4 cm^3/g) by CPM-7.3a-NiV, C_2H_4 (134.0 cm^3/g) and C_2H_6 (148.0 cm^3/g) by CPM-7.3a-CoV at 1 bar and 298 K and promising separation performance for gas mixtures such as C_2H_2/CO_2.

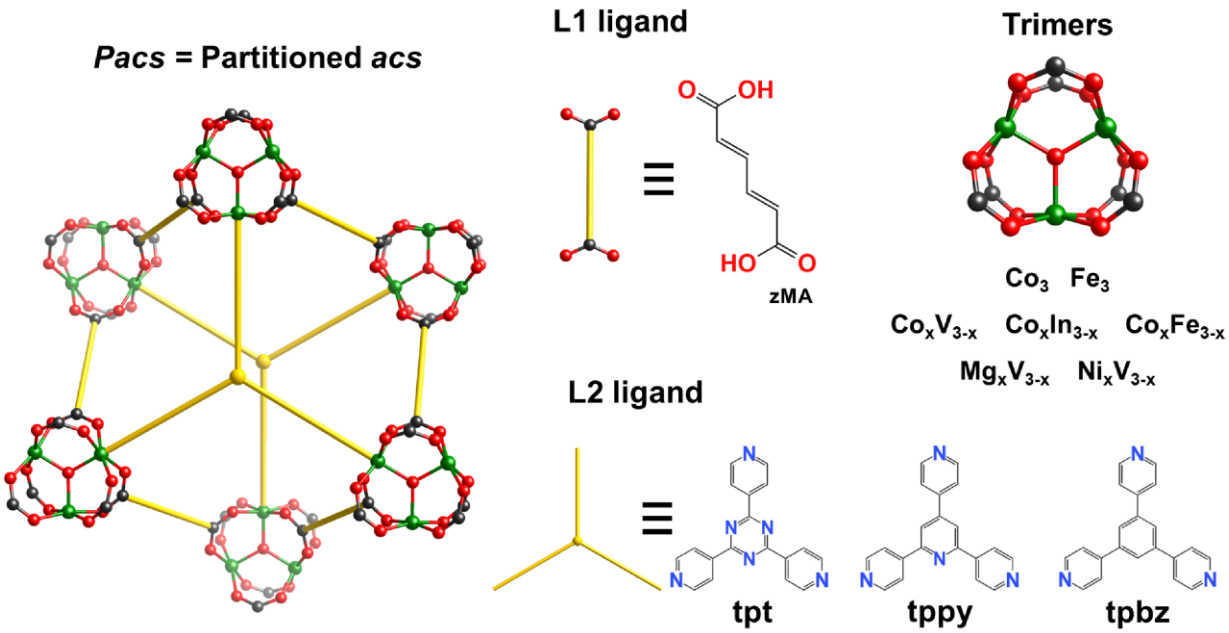

Figure 1. Illustration of isoreticular *pacs*-MOF with zMA (L1 ligand). Trimer and L2 ligand are the other two modules. Seven types of metal trimers and three types of L2 ligands are demonstrated on this zMA-*pacs* platform.

2. Results and Discussion

2.1. The scissoring and acyclic approach to the synthesis of pore-space-partitioned MOF materials

The *pacs* platform has been shown to be among the most versatile multi-module MOF platforms.[11-22] It consists of two ligand types. The ditopic ligand (called L1 ligand, usually dicarboxylate, diazolate, or their mixed ditopic varieties) functions as the framework-forming module to crosslink M_3(O/OH) trimers into MIL-88/MOF-235 *acs* topology[23-24] while a 3-connected ligand (called L2 ligand, usually a tripyridyl ligand) partitions the pore space through M-N coordinative bonds. The *pacs* materials were first developed using aromatic dicarboxylic acids such as 1,4-benzenedicarboxylate. The introduction of the BIS strategy extended the ligand type to non-aromatic, but still cyclic ligands such as bcp (bcp = bicyclo[1.1.1]pentane-1,3-dicarboxylate), bco, and cdc (cdc = 1,4-cubanedicarboxylate).[8, 25] All these cyclic ligands also tend to be rigid with the exception of monocyclic ligands such as chdc (chdc = *trans*-1,4-cyclohexanedicarboxylate) and tcb (tcb = *trans*-1,3-cyclobutanedicarboxylate).[7, 10] The use of rigid mono- and bi-cyclic ligands is prevalent in the MOF field for the simple reason that acyclic-ligand-based MOFs are more difficult to synthesize due to the conformational flexibility of acyclic ligands. On the other hand, as a multi-module platform that can use a rigid ligand (L2) to constrain the behavior of a less rigid ligand (L1), the pacs platform may offer a new opportunity to incorporate acyclic ligands. It has been clearly shown that there is a cooperative effect between M3-L1 and M3-L2 interactions that has made it possible to introduce chemical moieties (into pacs) that are not present elsewhere.

Very recently and concurrently with this work, the first acyclic ligand (fumaric acid) was introduced into the *pacs*.[26] Fumarate is an atypical acyclic ligand because its only two single bonds are attached to the functional groups. Such single bonds usually do not contribute much to the conformational flexibility. Thus fumarate is just as rigid as cyclic ligands such as bdc. Despite the success with fumarate, expanding the *pacs* materials to acyclic ligands remains a worthwhile pursuit. There is a high significance for the study of the *pacs* materials based on more flexible and/or less symmetrical ligands. For example, the reduction of the symmetry of *pacs* materials (topological symmetry $P6_3/mmc$) may be beneficial in some applications such as the use of the crystalline sponge method for the determination of unknown molecular structures.[27] The

conformationally flexible ligand also has the benefit of achieving induced fit upon the guest inclusion to allow more precise determination of the guest structure.

In this work, trans, trans-muconate is used as L1 ligand to build *pacs*-MOFs. Even with just one L1 ligand, many new *pacs* materials can be synthesized because of diverse metal-trimer compositions as well as availability of different L2 ligands, which is an advantage from the multi-module platform. Here we selectively demonstrate the synthesis of 9 new *pacs* materials that allow us to study both the effect from different L2 ligands as well as the effect from different metal trimers on gas sorption properties.

While trans, trans-muconic acid can be viewed as the scaled-up version of fumaric acid, from some perspectives, it is more appropriate to consider it as a scissored bdc ligand. The *pacs* chemistry of trans, trans-muconate is more similar to bdc ligand than to that of fumarate ligand. For example, both homometallic and heterometallic *pacs* materials can be made with zMA and bdc, whereas for fumarate ligand, only heterometallic compositions can be made on *pacs* so far.

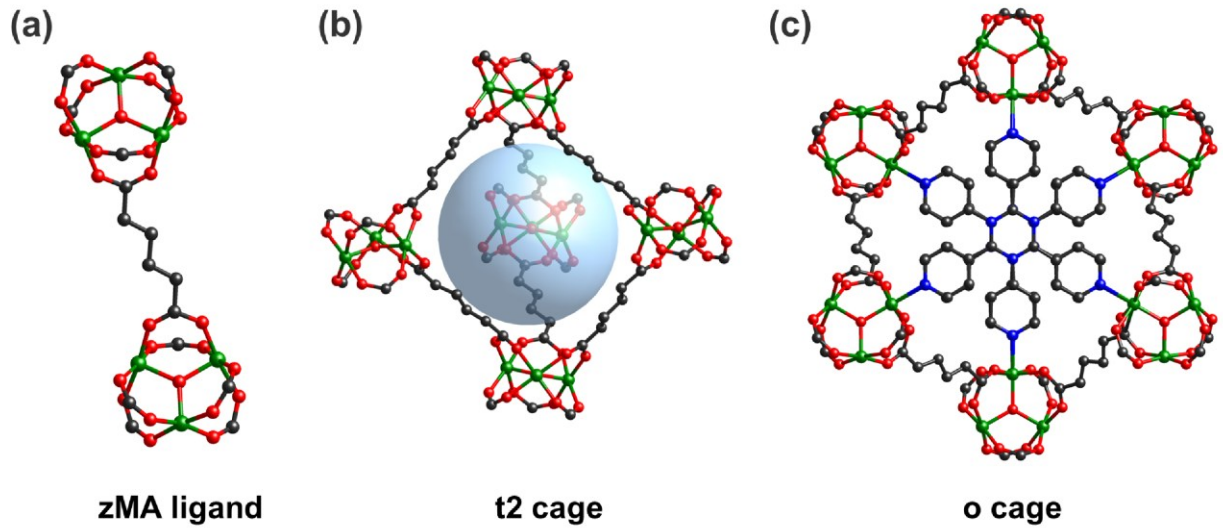

Figure 2. Crystal structure of CoV-zMA-tpt. (a) adjacent trimers have two-bond offset from zMA ligand, (b) trigonal bipyramidal cage (also called t2 cage), and (c) the octahedral cage (also called o cage).

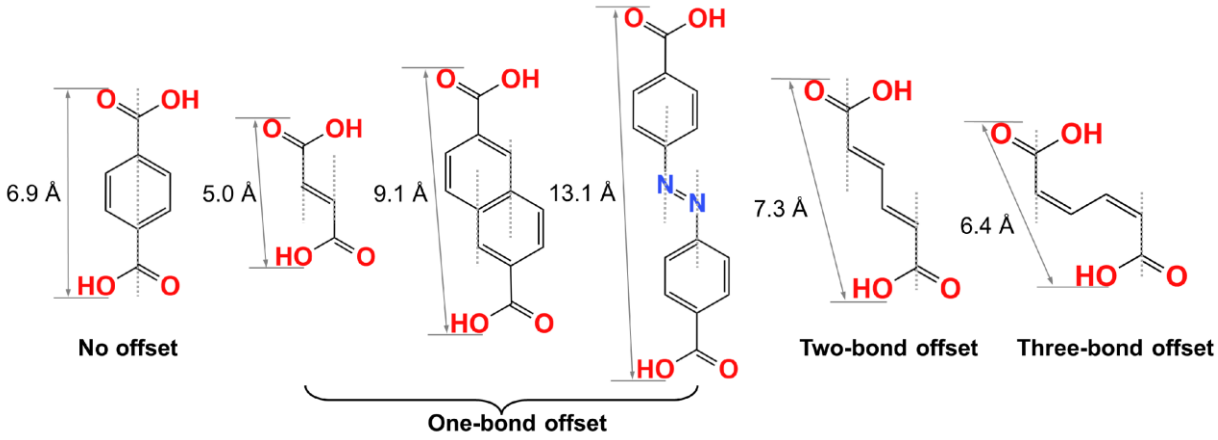

Scheme 2. Illustration of in-plane offsets between two -COO groups. It remains to be determined what is the maximum degree of offsets on the pacs platform before the breakdown of the isoreticular replacement strategy.

In these *pacs* materials, *trans*, *trans*-muconate adopts a z-shaped conformation with the maximum distance between two -COO groups (7.3 Å, denoted as zMA) (**Figure 2**), which helps fill the gap between two common dicarboxylates observed on the pacs platform (6.9 Å for bdc, 9.1 Å for 26ndc, 26ndc=2,6-naphthalenedicarboxylate). This zigzag shape of zMA (*path* length: 4 C atoms between two -COO groups) is similar to (but shorter than) 26ndc ligand (*path* length: 6 C atoms) whose *pacs* form is often reported in the space group *P*-31*c* (No. 163). The in-plane offset between two -COO groups (the distance between two planes bisecting two -COO groups) in zMA is larger than that in 26ndc. Put it another way, the two -COO groups in zMA are offset by two slanted C=C bonds whereas the two -COO groups in 26ndc are offset by just one slanted aromatic C-C bond (**Scheme 2**). Note that in common *pacs* materials, there is zero in-plane offset between two COO- groups. A larger offset may be less inducive to the formation of the *pacs*. In fact, the offset in zMA is the largest one achieved so far in the *pacs* materials. Note that the ratio between the offset length (perpendicular to the metal-ligand bonding vector) and the ligand length (parallel to the bonding vector) can play an important role on whether the *pacs* structure can be formed or not. A large ratio deviates more from the ideal pacs structure and is more likely to result in the

breakdown of isoreticular chemistry. For example, it has not been possible to make *pacs* materials from cis, cis-muconic acid (**Scheme 2**) even though the metal-ligand bonding vectors are parallel. The reason is not necessarily the large three-bond offset, but rather the large ratio between the offset length and the ligand length.

CPM-7.3 crystallized in *P*-3*c*1 space group (No. 165) due to the lower symmetry of zMA, which is in contrast with the space group *P*-31*c* (No. 163) often used for 26ndc *pacs* materials. It is the first time that a *pacs* material was found in this space group. Other trigonal/hexagonal space groups for *pacs* structures include $P6_3/mmc$ (No. 194), *P*-62c (No. 190), *P*-6*m*2 (No. 187), and $P6_3/m$ (No. 176). The highest possible symmetry for *pacs* materials is the $P6_3/mmc$ space group (No. 194) which occurs for most *pacs* materials made with sp^2-C-based cyclic L1 ligands (e.g., bdc) or sp^3-C-based bicyclic BIS-ligands (e.g., bcp, bco, cdc). It is worth noting that L1 is not the only factor that affects the lattice symmetry. Also the symmetry reduction in L1 does not necessarily lower the lattice symmetry due to possible L1 disorder. The symmetry of L1, the type of L1-L2 combinations, and the resulting interplay between L1 and L2 can also impact the lattice symmetry.

The unit cell of zMA-*pacs* is a 3-fold super cell with the trigonal space group. The super cell in zMA-*pacs* expand the *a*/*b* axis to √3 times compared to the regular *pacs* space group while keeping the *c* axis length essentially unchanged (**Table 1**). For comparison with the regular *pacs* structures, we also calculated the adjusted *a*/*b* lengths for zMA-*pacs* (multiplied by 1/√3, Figure S8). This enlargement of the unit cell volume is a route to reduce lattice symmetry which results from the lower symmetry of zMA ligand (C_{2h}), as compared to higher-symmetry ligands such as bdc (D_{2h}). Due to its zigzag shape, zMA lacks the mirror symmetry (the one that bisects -COO groups) that is present at the L1 site (2/*m*) in the highest topological symmetry of the *pacs* net ($P6_3/mmc$). The control of the framework symmetry, especially desymmetrization, can be an important aspect in creating unique host-guest chemistry for various applications, for example, as crystalline sponge to determine molecular structures of drug candidates that are impossible to crystallize by themselves.

Table 1. Summary of crystallographic data of all zMA-*pacs* in this work.

Sample code	Space group	*a* axis	*c* axis	Cell volume	*c*/*a* ratio
CoV-zMA-tpt	*P*-3*c*1	28.847(3)	15.407(2)	11103(3)	0.534
CoV-zMA-tpt[a]	*P*6$_3$/*mmc*	16.6553	15.407	3701	0.925
CoV-zMA-tppy[b]	*P*-3*c*1	29.051	15.792	11542.6	0.546
CoV-zMA-tppy[a, b]	*P*6$_3$/*mmc*	16.773	15.792	3847.5	0.942
CoV-zMA-tpbz	*P*-3*c*1	29.2445(13)	15.2542(13)	11298.2(12)	0.521
CoV-zMA-tpbz[b]	*P*6$_3$/*mmc*	16.8848	15.2542	3766.0	0.903
CoIn-zMA-tpt	*P*-3*c*1	29.0138(13)	15.7043(14)	11448.8(14)	0.541
CoIn-zMA-tpt[b]	*P*6$_3$/*mmc*	16.7516	15.7043	3816.3	0.937
CoFe-zMA-tpt	*P*-3*c*1	29.174	15.895	11715.5	0.545
CoFe-zMA-tpt[b]	*P*6$_3$/*mmc*	16.844	15.895	3,905.2	0.944
MgV-zMA-tpt	*P*-3*c*1	29.147(2)	15.3573(18)	11299(2)	0.527
MgV-zMA-tpt[b]	*P*6$_3$/*mmc*	16.8285	15.3573	3766.3	0.913
NiV-zMA-tpt[a]	*P*-3*c*1	28.681	15.727	11203.9	0.548
NiV-zMA-tpt[a, b]	*P*6$_3$/*mmc*	16.559	15.727	3734.63	0.950
Fe-zMA-tpt[a]	*P*-3*c*1	28.797	16.085	11552.3	0.559
Fe-zMA-tpt[a, b]	*P*6$_3$/*mmc*	16.626	16.085	3850.8	0.967

[a] *a*/*b* length of the super cell equal to $\sqrt{3}$ *a*/*b* length of regular *pacs* (*P*6$_3$/*mmc* space group).

[b] The unit cell parameters are calculated by powder X-ray diffraction data.

2.2. N_2 Adsorption and C_2H_2/CO_2 Uptake Capacity and Separation Properties of zMA-*pacs*

In this work, we focused on gas sorption properties of zMA-*pacs* materials based on heterometallic MgV, CoV and NiV compositions because these compositions often offer higher stability, likely due to their neutral or near-neutral frameworks. The *pacs* materials are desolvated by solvent exchange with acetone first, and followed by activation under high vacuum at 60 °C for 12 h. The gas sorption properties for N_2, CO_2, and C_2H_2 are summarized in **Table 2**. The BET (Brunauer-Emmett-Teller) surface areas of CoV-zMA-tpt, CoV-zMA-tppy, CoV-zMA-tpbz, MgV-zMA-tpt, and NiV-zMA-tpt are 1679, 1682, 1723, 1412 and 1678 m^2/g according to the N_2 sorption at 77 K (**Figure 3a**). In general, these values are higher than homometallic M(II)-bdc-tpt

pacs-MOFs with anionic frameworks such as Mg-bdc-tpt (956 m^2/g),[21] Mn-bdc-tpt (939 m^2/g),[28] Co-bdc-tpt (1008 m^2/g),[29] and Ni-bdc-tpt[30] (960 m^2/g) and are comparable to heterometallic bdc-tpt *pacs*-MOFs such as CoV-bdc-tpt (1603 m^2/g) and MgV-bdc-tpt[21] (1592 m^2/g). The difference could be attributed to the presence of the extra-framework charge-balancing species for anionic pacs materials. Additionally, BET surface areas of CoV-zMA-tpt (1679 m^2/g), CoV-zMA-tppy (1682 m^2/g) and CoV-zMA-tpbz (1723 m^2/g) are higher than corresponding heterometallic CoV-bdc-tpt (1603 m^2/g), CoV-bdc-tppy (1530 m^2/g) and CoV-bdc-tpbz (1630 m^2/g).[7] In addition to the surface area, heterometallic vanadium zMA-*pacs* shows large pore volume. The pore volume of CoV-zMA-tpt (0.651 cm^3/g), CoV-zMA-tppy (0.649 cm^3/g), and CoV-zMA-tpbz (0.645 cm^3/g), are also higher than bdc-*pacs* CoV-bdc-tpt (0.596 cm^3g), CoV-bdc-tppy (0.564 cm^3g) and CoV-bdc-tpbz (0.601 cm^3g).[7] The higher surface area and porosity of the zMA pacs materials compared to bdc-pacs materials are likely due to the longer zMA ligand (**Scheme 2**).

Table 2. Pore properties and C_2H_2, CO_2 sorption properties of **zMA-*pacs*** in this work.

		CoV-zMA-tpt	CoV-zMA-tppy	CoV-zMA-tpbz	MgV-zMA-tpt	NiV-zMA-tpt
BET surface area (m^2/g)		1679	1682	1723	1412	1678
Pore volume (cm^3/g)		0.651	0.649	0.645	0.531	0.654
Pore size distribution (Å)		6.3, 7.8	6.0, 7.8	5.9, 8.0	6.4, 7.8	5.9, 7.7
CO_2 at 1 bar (cm^3/g)	298K	69.2	72.3	74.5	64.3	81.3
	273K	144.9	142.0	151.7	136.7	153.8
CO_2 Q^0_{st} (-kJ/mol)		19.9	19.7	19.2	20.8	17.8
C_2H_2 at 1 bar (cm^3/g)	298K	150.3	152.2	147.0	145.6	165.4
	273K	221.3	212.6	218.4	213.5	229.1
C_2H_2 Q^0_{st} (-kJ/mol)		28.0	26.2	23.9	26.4	27.2
C_2H_2/CO_2 selectivity (298 K, 1bar)		3.6	3.7	3.6	3.9	4.0
Separation potential (mmol/g)		3.24	3.38	3.33	3.28	4.05

The CO_2 uptakes at 298 K and 1 bar are high compared to most reported MOF materials (**Figure 3b**) and are 69.2 for CoV-zMA-tpt, 72.3 for CoV-zMA-tppy, 74.5 for CoV-zMA-tpbz, 64.3 for MgV-zMA-tpt, and 81.3 cm^3/g for NiV-zMA-tpt. CO_2 uptake of CoV-zMA-tpt is comparable with

some CO_2 adsorption materials.[31-33] Additionally, CoV-zMA-L2 *pacs* and NiV-zMA-tpt shows high C_2H_2 uptakes (**Figure 3c**). The C_2H_2 uptakes of CoV-zMA-tpt, CoV-zMA-tppy, CoV-zMA-tpbz are 150.3 and 152.2, and 147.0 at 298 K and 1 bar, slightly lower than CoV-bdc-*pacs* such as CoV-bdc-tpt (162.0 m^2/g), CoV-bdc-tppy (164.3 m^2/g) and CoV-bdc-tpbz (164.7 m^2/g).[7] However, NiV-zMA-tpt has C_2H_2 uptake (165.4 cm^3/g) that is slightly higher than CoV-bdc-*pacs*.

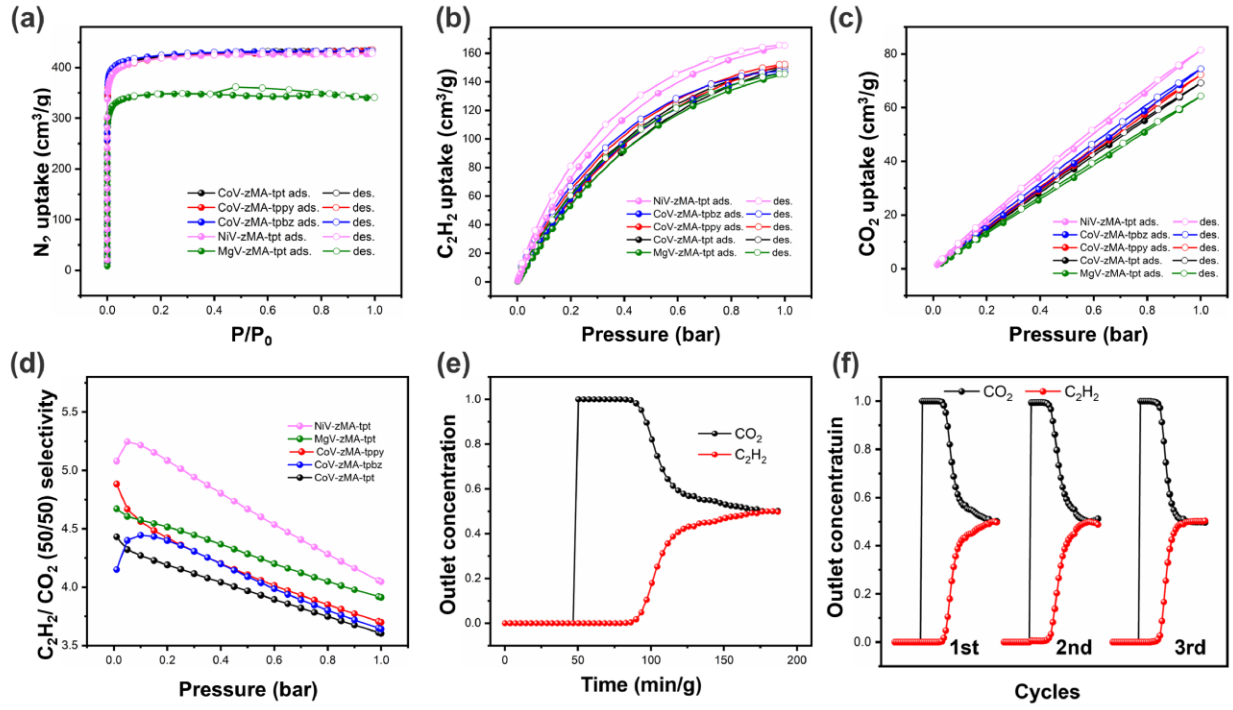

Figure 3. (a) N_2 sorption isotherms of zMA-*pacs* at 77 K. (b) (c) C_2H_2 and CO_2 sorption isotherms at 298 K. (d) C_2H_2/CO_2 selectivity (50:50) for 298 K. (e) C_2H_2 and CO_2 mixture breakthrough curves for CoV-zMA-tpt and (f) 3 cycles of breakthrough measurements.

The isotherms of C_2H_2 and CO_2 at 298 K were used to fit with the Dual-Site Langmuir-Freundlich (DSLF) model to calculate the ideal adsorbed solution theory (IAST, 50/50) selectivity. The C_2H_2/CO_2 selectivity of CoV-zMA-tpt, CoV-zMA-tppy and CoV-zMA-tpbz are 3.6, 3.7 and 3.6 (**Figure 3d**) which is comparable with some C_2H_2/CO_2 separation MOF materials.[32-33] NiV-zMA-tpt has a higher selectivity of 4.0 and shows potentially better separation property than CoV-zMA *pacs*. These selectivity values are higher than CoV-bdc-tpt (2.6), CoV-bdc-tppy (2.8) and

CoV-bdc-tpbz (2.7). The separation potential of CoV-zMA-tpt, CoV-zMA-tppy, CoV-zMA-tpbz and NiV-zMA-tpt are 3.24, 3.38, 3.33 and 4.05 mmol/g, all of which are higher than CoV-bdc-tpt (2.7 mmol/g), indicating better C_2H_2/CO_2 separation property of zMA-*pacs* than bdc-*pacs*. The separation potential of NiV-zMA-tpt (4.05 mmol/g) is higher than many reported MOFs such as FeNi-M'MOF (3.8 mmol/g), CPM-110c-CoV (3.6 mmol/g),[7] ZJU-74a (3.1 mmol/g), BSF-3 (2.8 mmol/g), JCM-1 (2.4 mmol/g) and SNNU-29-Mn (2.4 mmol/g).

Dynamic breakthrough curves were obtained for CoV-zMA-tpt on a fixed-bed column to evaluate the practical C_2H_2 over CO_2 separation performance. As shown in **Figure 3e**, CO_2 first flowed out of the fixed bed and then C_2H_2 was detected for additional ~33 min/g, which is consistent with the C_2H_2-selective separation as calculated from IAST predication. The C_2H_2/CO_2 breakthrough time is longer than many benchmark MOF materials with the same gas flow rate (2 mL/min), such as UTSA-300a[34] (12 min g^{-1}) and FJU-90a[35] (22 min g^{-1}), and is comparable to ZJU-74a[36] (36 min g^{-1}). Multicycle mixed-gas breakthrough experiments were measured under the same conditions. As shown in **Figure 3f**, breakthrough time is the same for three runs of experiment, which confirms the material stability of CoV-zMA-tpt for C_2H_2/CO_2 gas separation.

2.3. C_2H_6/C_2H_4 and C_3H_6/C_3H_8 Uptake Capacity and Separation Properties of zMA-*pacs*

We also studied gas uptake and separation properties of other C2 gases (C_2H_4 and C_2H_6) using CoV-zMA-tpt. CoV-zMA-tpt adsorbs 148.0 cm^3/g and 185.5 cm^3/g C_2H_6 gas at 298 K and 273 K at 1 bar (**Figure 4a, b**). This C_2H_6 uptake is higher than the vast majority of MOF materials such as UPC-66a (60.9 cm^3/g),[37] PCN-250 (116.7 cm^3/g),[38] $Ni(BDC)(TED)_{0.5}$ (112 cm^3/g),[39] MUF-15 (105.1 cm^3/g), IRMOF-8 (92 cm^3/g),[40] CoV-ndc-tpt (90.2 cm^3/g),[16] MIL-142A (85.1 cm^3/g),[41] $Fe_2(O_2)(DOBDC)$ (74.3 cm^3/g),[42] PCN-245 (73.2 cm^3/g),[40] ZIF-4 (51.5 cm^3/g),[43] ZIF-8 (45.4 cm^3/g),[44] $Cu(Qc)_2$[34] (41.5 cm^3/g) and MAF-49[45] (38.8 cm^3/g) at 298 K and 1 bar.

The C_2H_4 uptake is 134.0 and 181.7 cm^3/g at 298, 273 K and 1 bar (**Figures 4a, b**). Interestingly, the C_2H_4 uptake of CoV-zMA-tpt is lower than the C_2H_6 uptake, giving rise to C_2H_6-selective property for the C_2H_4/C_2H_6 gas mixture. The calculated IAST selectivity of CoV-zMA-tpt is 1.54

and 1.55 at 298, 273 K and 1 bar (**Figure 4c-e**). The selectivity is higher than CoV-26ndc-tpt (1.48),[16] MIL-142A (1.51),[41] TJT-100 (1.49),[46] and V-bdc-tpt (1.43),[11] but lower than some high C_2H_6-selective MOF materials such as $Fe_2(O_2)$(DOBDC) (4.4),[42] $Cu(Qc)_2$ (3.41),[47] PCN-250 (1.9),[38] and CoV-bdc-tpt[16] (1.75) at 298 K and 1 bar. The separation potential at 273 K is 1.77 mmol/g (**Figure 4f**), higher than that (1.35 mmol/g) at 298 K, implies the better separation property at lower temperature for zMA-*pacs*. The separation potential (1.35 mmol/g) of CoV-zMA-tpt at 298 K and 1 bar is higher than many C_2H_6-selective MOF materials such as V-bdc-tpt (1.29 mmol/g),[11] SNNU-40 (1.27 mmol/g), $Ni(BDC)(TED)_{0.5}$ (1.01 mmol/g), $Cu(Qc)_2$ (0.85 mmol/g),[47] ZIF-4 (0.83 mmol/g),[43] and PCN-245[40] (0.80 mmol/g) due to the very high C_2H_6 uptake of CoV-zMA-tpt.

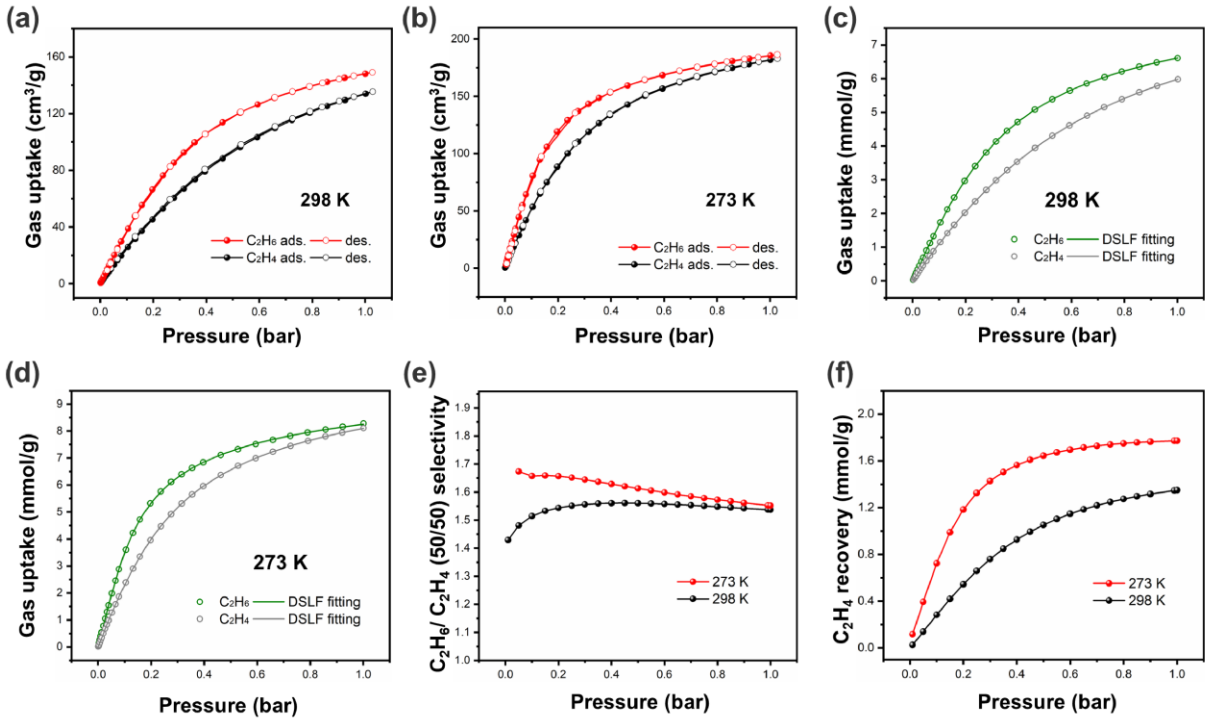

Figure 4. C_2H_6 and C_2H_4 sorption properties of CoV-zMA-tpt. (a) (b) C_2H_6 and C_2H_4 sorption isotherms at 298 K and 273 K, respectively. (c) (d) DSLF fitting of C_2H_6 and C_2H_4 isotherms at 298 K and 273 K, respectively. (e) (f) Selectivity and separation potential to C_2H_6/C_2H_4 (50/50) at different temperatures.

Additionally, CoV-zMA-tpt shows C_3H_6-selective C_3H_6/C_3H_8 separation selectivity of 1.04 at 298 K and 1 bar with the separation potential of 0.145 mmol/g. The separation property improved at lower temperature to 1.28 for the selectivity and 1.02 mmol for separation potential at 273 K (**Figure 5**).

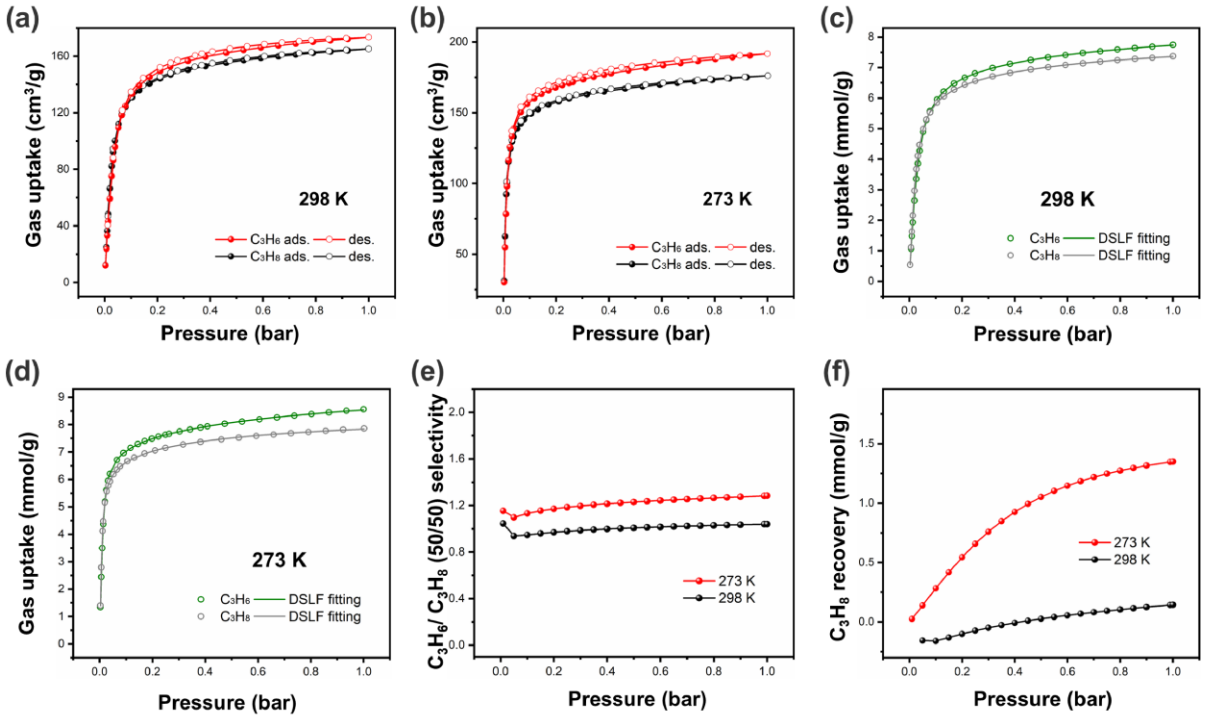

Figure 5. C_3H_6 and C_3H_8 sorption properties of CoV-zMA-tpt. (a) (b) C_3H_6 and C_3H_8 sorption isotherms at 298 K and 273 K, respectively. (c) (d) DSLF fitting of C_3H_6 and C_3H_8 isotherms at 298 K and 273 K, respectively. (e) (f) Selectivity and separation potential to C_3H_6/C_3H_8 (50/50) at different temperatures.

3. Conclusion

With the successful synthesis of a family of new porous zMA-pacs materials, this work demonstrates the great promise of acyclic ligands for the construction of highly porous and stable crystalline porous materials. As shown here, these new materials have gas sorption and separation properties that are superior to the vast majority of MOFs made from both cyclic and acyclic ligands.

This work will help inspire a renewed enthusiasm on the chemistry of MOF materials from acyclic ligands and their applications.

Supporting Information

Supporting Information is available from the Wiley Online Library or from the author. Detail experimental procedures, materials characterization, single crystallographic parameters, and gas sorption data are included in supporting information.

Acknowledgements

This work was supported by National Science Foundation, Division of Materials Research, under Award # 2105961 (X. B.). Single-crystal X-ray diffraction studies were performed on an instrument purchased with an NSF MRI grant (CHEM 2117040, X.B.). X.B. thanks CSULB for the RSCA award for 3-unit teaching release time.

Reference

[1] M. Eddaoudi, J. Kim, N. Rosi, D. Vodak, J. Wachter, M. O'Keeffe, O. M. Yaghi, *Science* **2002**, *295*, 469-472.
[2] S.-C. Fan, Y.-L. Zhang, J.-J. Ni, Y.-P. Li, S.-N. Li, Q.-G. Zhai, *Inorg. Chem.* **2023**, *62*, 20279-20287.
[3] A. N. Hong, Y. Wang, Y. Chen, H. Yang, E. Kusumoputro, X. Bu, P. Feng, *Chem. Eur. J.* **2023**, *29*, e202203547.
[4] A. N. Hong, E. Kusumoputro, Y. Wang, H. Yang, Y. Chen, X. Bu, P. Feng, *Angew. Chem. Int. Ed.* **2022**, *61*, e202116064.
[5] L. K. Macreadie, E. J. Mensforth, R. Babarao, K. Konstas, S. G. Telfer, C. M. Doherty, J. Tsanaktsidis, S. R. Batten, M. R. Hill, *J. Am. Chem. Soc.* **2019**, *141*, 3828-3832.
[6] V. Guillerm, T. Grancha, I. Imaz, J. Juanhuix, D. Maspoch, *J. Am. Chem. Soc.* **2018**, *140*, 10153-10157.
[7] W. Wang, H. Yang, Y. Chen, X. Bu, P. Feng, *J. Am. Chem. Soc.* **2023**, *145*, 17551-17556.
[8] H. Yang, Y. Chen, C. Dang, A. N. Hong, P. Feng, X. Bu, *J. Am. Chem. Soc.* **2022**, *144*, 20221-20226.
[9] M. A. M. Subbaiah, N. A. Meanwell, *J. Med. Chem.* **2021**, *64*, 14046-14128.
[10] Y. Xiao, Y. Chen, W. Wang, H. Yang, A. N. Hong, X. Bu, P. Feng, *J. Am. Chem. Soc.* **2023**, *145*, 10980-10986.
[11] W. Wang, Y. Chen, P. Feng, X. Bu, *Adv. Mater.* **2024**, *36*, 2403834.
[12] P. Ajayan, W. Wang, Y. Chen, X. Bu, P. Feng, *Adv. Mater.* **2024**, *36*, 2408042.
[13] Y. Chen, H. Yang, W. Wang, X. Li, Y. Wang, A. N. Hong, X. Bu, P. Feng, *Small* **2023**, *19*, 2303540.
[14] A. N. Hong, H. Yang, X. Bu, P. Feng, *EnergyChem* **2022**, *4*, 100080.
[15] A. N. Hong, H. Yang, T. Li, Y. Wang, Y. Wang, X. Jia, A. Zhou, E. Kusumoputro, J. Li, X. Bu, P. Feng, *ACS Appl. Mater. Interfaces* **2021**, *13*, 52160-52166.

[16] H. Yang, Y. Wang, R. Krishna, X. Jia, Y. Wang, A. N. Hong, C. Dang, H. E. Castillo, X. Bu, P. Feng, *J. Am. Chem. Soc.* **2020**, *142*, 2222-2227.

[17] Y. Wang, X. Zhao, H. Yang, X. Bu, Y. Wang, X. Jia, J. Li, P. Feng, *Angew. Chem. Int. Ed.* **2019**, *58*, 6316-6320.

[18] Q.-G. Zhai, X. Bu, X. Zhao, D.-S. Li, P. Feng, *Acc. Chem. Res.* **2017**, *50*, 407-417.

[19] X. Zhao, C. Mao, K. T. Luong, Q. Lin, Q.-G. Zhai, P. Feng, X. Bu, *Angewandte Chemie International Edition* **2016**, *55*, 2768-2772.

[20] X. Zhao, X. Bu, E. T. Nguyen, Q.-G. Zhai, C. Mao, P. Feng, *J. Am. Chem. Soc.* **2016**, *138*, 15102-15105.

[21] Q.-G. Zhai, X. Bu, C. Mao, X. Zhao, L. Daemen, Y. Cheng, A. J. Ramirez-Cuesta, P. Feng, *Nat. Commun.* **2016**, *7*, 13645.

[22] H. Yang, F. Peng, A. N. Hong, Y. Wang, X. Bu, P. Feng, *J. Am. Chem. Soc.* **2021**, *143*, 14470-14474.

[23] S. Surblé, C. Serre, C. Mellot-Draznieks, F. Millange, G. Férey, *Chem. Commun.* **2006**, 284-286.

[24] A. C. Sudik, A. P. Côté, O. M. Yaghi, *Inorg. Chem.* **2005**, *44*, 2998-3000.

[25] Y. Xiao, A. N. Hong, Y. Chen, H. Yang, Y. Wang, X. Bu, P. Feng, *Small* **2023**, *19*, 2205119.

[26] Y. Chen, W. Wang, S. Alston, Y. Xiao, P. Ajayan, X. Bu, P. Feng, *Angew. Chem. Int. Ed.* **2024**, *n/a*, e202415576.

[27] Y. Inokuma, S. Yoshioka, J. Ariyoshi, T. Arai, Y. Hitora, K. Takada, S. Matsunaga, K. Rissanen, M. Fujita, *Nature* **2013**, *495*, 461-466.

[28] T. Zhang, J.-W. Cao, Y.-F. Dai, H. Feng, S.-Y. Zhang, J. Chen, T. Wang, Y. Wang, K.-J. Chen, *Crystal Growth & Design* **2022**, *22*, 3594-3600.

[29] T. Zhang, Y.-Q. Hu, T. Han, Y.-Q. Zhai, Y.-Z. Zheng, *ACS Appl. Mater. Interfaces* **2018**, *10*, 15786-15792.

[30] X. Zhao, X. Bu, Q.-G. Zhai, H. Tran, P. Feng, *J. Am. Chem. Soc.* **2015**, *137*, 1396-1399.

[31] W. Fan, H. Lin, X. Yuan, F. Dai, Z. Xiao, L. Zhang, L. Luo, R. Wang, *Inorg. Chem.* **2016**, *55*, 6420-6425.

[32] X. Feng, X. Wang, H. Yan, H. Liu, X. Liu, J. Guan, Y. Lu, W. Fan, Q. Yue, D. Sun, *Angew. Chem. Int. Ed.* **2024**, *63*, e202407240.

[33] W. Fan, S. Yuan, W. Wang, L. Feng, X. Liu, X. Zhang, X. Wang, Z. Kang, F. Dai, D. Yuan, D. Sun, H.-C. Zhou, *J. Am. Chem. Soc.* **2020**, *142*, 8728-8737.

[34] R.-B. Lin, L. Li, H. Wu, H. Arman, B. Li, R.-G. Lin, W. Zhou, B. Chen, *J. Am. Chem. Soc.* **2017**, *139*, 8022-8028.

[35] Y. Ye, Z. Ma, R.-B. Lin, R. Krishna, W. Zhou, Q. Lin, Z. Zhang, S. Xiang, B. Chen, *J. Am. Chem. Soc.* **2019**, *141*, 4130-4136.

[36] J. Pei, K. Shao, J.-X. Wang, H.-M. Wen, Y. Yang, Y. Cui, R. Krishna, B. Li, G. Qian, *Adv. Mater.* **2020**, *32*, 1908275.

[37] Y. Wang, M. Fu, S. Zhou, H. Liu, X. Wang, W. Fan, Z. Liu, Z. Wang, D. Li, H. Hao, X. Lu, S. Hu, D. Sun, *Chem* **2022**, *8*, 3263-3274.

[38] Y. Chen, Z. Qiao, H. Wu, D. Lv, R. Shi, Q. Xia, J. Zhou, Z. Li, *Chem. Eng. Sci.* **2018**, *175*, 110-117.

[39] W. Liang, F. Xu, X. Zhou, J. Xiao, Q. Xia, Y. Li, Z. Li, *Chem. Eng. Sci.* **2016**, *148*, 275-281.

[40] D. Lv, R. Shi, Y. Chen, Y. Wu, H. Wu, H. Xi, Q. Xia, Z. Li, *ACS Appl. Mater. Interfaces* **2018**, *10*, 8366-8373.

[41] Y. Chen, H. Wu, D. Lv, R. Shi, Y. Chen, Q. Xia, Z. Li, *Ind. Eng. Chem. Res.* **2018**, *57*, 4063-4069.

[42] L. Li, R.-B. Lin, R. Krishna, H. Li, S. Xiang, H. Wu, J. Li, W. Zhou, B. Chen, *Science* **2018**, *362*, 443-446.

[43] M. Hartmann, U. Böhme, M. Hovestadt, C. Paula, *Langmuir* **2015**, *31*, 12382-12389.

[44] U. Böhme, B. Barth, C. Paula, A. Kuhnt, W. Schwieger, A. Mundstock, J. Caro, M. Hartmann, *Langmuir* **2013**, *29*, 8592-8600.

[45] P.-Q. Liao, W.-X. Zhang, J.-P. Zhang, X.-M. Chen, *Nat. Commun.* **2015**, *6*, 8697.

[46] H.-G. Hao, Y.-F. Zhao, D.-M. Chen, J.-M. Yu, K. Tan, S. Ma, Y. Chabal, Z.-M. Zhang, J.-M. Dou, Z.-H. Xiao, G. Day, H.-C. Zhou, T.-B. Lu, *Angew. Chem. Int. Ed.* **2018**, *57*, 16067-16071.

[47] R.-B. Lin, H. Wu, L. Li, X.-L. Tang, Z. Li, J. Gao, H. Cui, W. Zhou, B. Chen, *J. Am. Chem. Soc.* **2018**, *140*, 12940-12946.